The Electrochemical Society
Advancing solid state & electrochemical science & technology

Size-dependent Electrochemical Properties of Binary Solid Solution Nanoparticles

Size-dependent Electrochemical Properties of Binary Solid Solution Nanoparticles

Hongxin Ma,[1,2] Panpan Gao,[1,3] Ping Qian,[1,3,z] and Yanjing Su[1,2,z]

[1]*Beijing Advanced Innovation Center for Materials Genome Engineering, University of Science and Technology Beijing, Beijing, 100083, People's Republic of China*
[2]*Corrosion and Protection Center, University of Science and Technology Beijing, Beijing 100083, People's Republic of China*
[3]*Department of Physics, University of Science and Technology Beijing, Beijing 100083, People's Republic of China*

The electrochemical properties have different or reverse trend with decreasing radius dependent on the synthetic methods and thermodynamic states of nanoparticles. Here, a size-dependent thermodynamic model was derived to describe the thermodynamic equilibrium state of binary solid solution nanoparticles. This model combined the capillary equation with the Gibbs-Duhem equation and the Butler-Volmer equation, can simultaneously analyze nanoparticle size, stresses, solute segregation and electrochemical properties in solid solution nanoparticles. Then, spherical nanoparticles of CuZn binary solid solution were studied. With decreasing CuZn nanoparticle radius, the anodic current density decreased, whereas the equilibrium potential increased, meaning that the stability was enhanced. With increasing apparent Zn concentration, the anodic current density and the equilibrium potential difference between the CuZn nanoparticle components increased, implying that the selective corrosion of Zn atoms enhanced. These results were qualitatively consistent with some experimental observations.
© 2020 The Electrochemical Society ("ECS"). Published on behalf of ECS by IOP Publishing Limited. [DOI: 10.1149/1945-7111/ab6ff1]

The most remarkable characteristic of nanomaterials is that the surface-to-volume ratio of these materials is much larger than that of bulk materials. The surface plays a key role in many thermodynamic processes, including electrochemical and chemical responses. Many researchers[1–7] have investigated the surface stress/energy of solid materials and have concluded that the surface stress is size dependent, especially for nanoscale materials. Dingreville et al.[6] concluded that the overall elastic behaviors of structural elements (particles, wires, and films) are size dependent. Zhang et al.[8] proposed an eigenstress model and showed that the initial deformation, surface energy density and surface stress are all dependent on the nanoscale film thickness, whereas surface elastic constants are independent of this thickness. Although the size dependence is negligible for conventional structural elements, this dependence will be significant for samples with at least one dimension on the nanoscale.

Moreover, many studies have verified that the solubility of solute atoms in nanoscale materials is size dependent.[9–14] The Au nanoparticles with 5 nm diameter showed an uptake of carbon to concentrations exceeding the bulk solubility by more than four orders of magnitude.[12] Meethong et al.[15] found that at room temperature, the Li solid solution limit in the heterosite phase Li_yFePO_4 increased as the particle diameter decreased from 113 nm to 42 nm and 34 nm, whereas the corresponding limit in the triphylite phase $Li_{1-x}FePO_4$ decreased. The authors attributed the size-dependent results to two origins: 1) surface energy and surface stress and 2) coherency or compatibility stresses in two-phase particles with coherent interfaces. Based on the adsorption isotherm, Zhang and Ren developed a Gibbs approach for grain boundary segregation in nanograined polycrystals[16] and surface segregation in nanoparticles[17] and concluded that the stresses and solute concentrations in nanostructures are size dependent.

Many numerical and experimental results have shown that the electrochemical properties of nanoscale metallic materials are size dependent.[18–23] The breakdown potential of nanograined (8–28 nm) and bulk nickel systematically increased from 1110 mV to 1540 mV (Ag-AgCl reference electrode) with decreasing grain size to 8 nm.[24] The oxidation potentials of Au[25] and Pd[26] nanoparticles were reported much more negative relative to the value for bulk Au and Pd, respectively. The presence of external mechanical, point defects and solute atoms influences the electrode reactions. Despite having

the same chemical composition, the breakdown potential of the sputtered nanocrystalline (grain size of approximately 25 nm) film of 304 stainless steel is approximately 850 mV higher than that of the conventional material.[27] Solute concentrations that are larger than certain values may lead to selective corrosion or galvanic corrosion of alloy materials, such as brass dezincification corrosion.[28–32]

Nanomaterials exhibit fascinating size-dependent properties have stimulated extensive interests in the catalytic, energy storage, batteries and corrosion researches. In order to describe the electrode reactions in various materials, many researchers derived the classic Butler-Volmer equation.[33–37] Gutman[38] and Ganser[39] systematically studied the influence of mechanics, and Yang[40] considered the effects of local stress and the radius of electrode surface curvature to develop a generalized Butler-Volmer relationship. However, electrochemical properties have different or reverse trend with decreasing diameter dependent on the synthetic methods and thermodynamic states of nanostructures. In contrast to these mentioned above, the corrosion resistance of the $Cu_{90}Ni_{10}$ alloy in neutral Cl^--containing solution was reduced when the grain size decreased to the nanoscale.[41] Whereas, the Cu[42] and Ag[43] nanoparticles showed an enhanced stability against anodic dissolution relative to that of bulk Cu and Ag, respectively. In this paper, the size-dependent electrochemical properties of nanoparticles and the influences of size-dependent stresses and solute concentrations was studied based on the thermodynamic equilibrium theory. Then spherical nanoparticles of CuZn binary solid solution were analyzed as examples.

Stresses and Solute Concentrations in Nanoparticles

Because of surface stress, free-standing nanomaterials subjected to no external loads will relax spontaneously to reach the thermodynamic equilibrium state, meeting energy minimization requirements, and introducing an initial deformation[8,17] not present in their strain-free bulk counterparts. Since the atoms within a very thin layer near the surfaces experience a different local environment from that of the atoms in bulk, the physical properties and mechanical responses of surfaces and bulk counterparts will be distinct. Usually, there are three common approaches to study the properties of surfaces[16,17]: the sharp surface approach, the diffusive surface approach and the interphase approach. Both diffusive surface and interphase approaches treat surfaces as three-dimensional (3D) surfaces. The interphase approach treats an interface as a thermodynamic phase and usually chooses locations where the properties

no longer vary significantly with respect to the position. The interphase surface has a finite volume (thickness) and may be assigned thermodynamic properties in a normal way.

Here, a spherical model with a core coherently bonded to a surface shell was employed. The 3D core and surface shell are both assumed to be mechanically isotropic and homogeneous. Since the surface thickness is small, a biaxial stress field with zero radial stress ($\sigma_x = \sigma_y$ and $\sigma_z = 0$) was assumed in the surface shell, whereas with a homogeneous triaxial stress field ($\sigma_x = \sigma_y = \sigma_z$) was assumed in the core. Usually, various defects may be induced into nanoparticles during fabrication processes. For simplicity, only the core, surface shell, stresses and solute atoms in the core and surface shell are considered; other defects are not analyzed here. Strain-free pure metallic nanoparticle was taken as the reference state, in which the core has an original radius of R_{c0} and the surface shell has an original thickness of Ω_0.

Many researchers have studied the initial deformation, stresses and solute segregations of nanomaterials. In particular, Zhang et al. systematically studied the interactions between interfacial stress and interfacial segregation in nanograined[16] and nanoparticle[17] materials. Based on the referenced pure metallic core–shell spherical model of nanoparticles discussed above, some second component atoms can be introduced into the core and surface shell as solute atoms to study binary solid solution nanoparticles. Obviously, these introduced solute atoms in the metallic nanoparticles will lead to additional deformations and stress variations in the surface shell and core. The volume of a solid solution can be described by a function of temperature, hydrostatic stress and composition. The change in the total volume can be expressed as the sum of volume changes in the core and surface shell $\Delta V = \Delta V_c + \Delta V_s$. Because the surface shell is coherently bounded with the core, based on the continuum mechanics theory, the tangential surface area strain should be equal to twice the lattice strain in the core $\frac{\Delta A_s}{A_{s,0}} = 2\frac{\Delta a}{a_0}$, where $A_{s,0}$ and ΔA_s denote the initial surface area and the change of surface areas, respectively; a_0 and Δa are the initial lattice constant and the change of lattice constant in the core, respectively.[16,17] Moreover, at the equilibrium state, the energy minimization requirements will yield the generalized capillary equation,[5,44,45] which could describe the mechanical force balance of spherical nanoparticles between the surface shell and core.

Based on these assumptions, Zhang et al.[17] obtained the relationships of stresses and solute concentrations in the surface shell and core of binary solid solution nanoparticles, which are expressed as

$$\frac{\Delta a}{a_0} = \frac{-2\sigma_s^0\Omega_0 + K_c^s R_{c,0}\frac{\bar{V}_c^s}{V_c}\frac{x_c^s}{1-x_c^s} + \frac{2}{3}\frac{\bar{V}_s^s}{V_s}\frac{x_s^s}{1-x_s^s}Y_s^s\Omega_0}{3K_c^s R_{c,0} + 2Y_s^s\Omega_0} \quad [1]$$

$$\sigma_s = \frac{3\sigma_s^0 K_c^s R_{c,0} + K_c^s R_{c,0}Y_s^s\left(\frac{\bar{V}_c^s}{V_c}\frac{x_c^s}{1-x_c^s} - \frac{\bar{V}_s^s}{V_s}\frac{x_s^s}{1-x_s^s}\right)}{3K_c^s R_{c,0} + 2Y_s^s\Omega_0} \quad [2]$$

$$\sigma_c = -2\frac{\Omega_0}{R_{c,0}}\sigma_s = \frac{-6\sigma_s^0\Omega_0 K_c^s + 2Y_s^s\Omega_0 K_c^s\left(\frac{\bar{V}_s^s}{V_s}\frac{x_s^s}{1-x_s^s} - \frac{\bar{V}_c^s}{V_c}\frac{x_c^s}{1-x_c^s}\right)}{3K_c^s R_{c,0} + 2Y_s^s\Omega_0} \quad [3]$$

where σ_s^0 is the surface biaxial eigenstress[8]; σ_c and σ_s are the stresses in the core and surface shell, respectively; K_c^s is the isothermal solute-related bulk modulus; $\bar{Y}_s^s$ and $Y_s^s = \frac{Y_s^s}{1-\nu}$ are the surface solute-related uniaxial and biaxial Young's modulus, respectively; and ν is the surface solute-related Poisson's ratio. Here, $\bar{V}_c^s = (\partial V_c/\partial n_c^s)_{\sigma_c}$ and $\bar{V}_s^s = (\partial V_s/\partial n_s^s)_{\sigma_s}$ are the partial molar volumes of solute atoms in the core and surface shell, respectively, which are assumed to be constant and independent of the solute mole number and hydrostatic stress. Furthermore, n_c^s and n_s^s are the mole numbers of solute atoms in the core and surface shell, respectively, and $x_c^s = n_c^s/(n_c^s + n_c)$ and $x_s^s = n_s^s/(n_s^s + n_s)$ are the solute concentrations of the core and

surface shell, respectively. In these expressions, $n_c = V_{c,0}/\underline{V}_c$ and $n_s = V_{s,0}/\underline{V}_s$ are the mole numbers of solvent atoms in the core and surface shell, respectively; $\underline{V}_c$ and $\underline{V}_s$ are the solute-free molar volume of atoms in the core and surface shell, respectively; and $V_{c,0}$ and $V_{s,0}$ are the volume of the core and surface shell in the referenced strain-free pure nanoparticle, respectively. Obviously, from Eqs. 1 and 3, the lattice strain and the stress in the surface shell and core are both functions of particle radius and solute concentrations.

For pure metallic nanoparticles, $x_c^s = 0$ and $x_s^s = 0$; thus, the lattice strain in Eq. 1 would be reduced to the initial strain ε^{ini}.

$$\varepsilon^{ini} = -\frac{2\sigma_s^0\Omega}{2Y_s\Omega + 3K_cR_c} \quad [4]$$

The stress in the surface shell and core of Eqs. 2 and 3 would be reduced to

$$\bar{\sigma}_s = \sigma_s^0 + Y_s\varepsilon^{ini} = \sigma_s^0\left(1 - \frac{2Y_s\Omega}{2Y_s\Omega + 3K_cR_c}\right) = \frac{3K_cR_c\sigma_s^0}{2Y_s\Omega + 3K_cR_c} \quad [5]$$

$$\bar{\sigma}_c = K_c e = 3K_c\varepsilon^{ini} = -\frac{6K_c\Omega\sigma_s^0}{2Y_s\Omega + 3K_cR_c} = -2\frac{\Omega}{R_c}\sigma_s \quad [6]$$

where ε denotes the linear strain of the core or the tangential direction linear strain of the surface, Y_s is the biaxial Young's modulus[8] in the surface shell, and K_c is the bulk modulus of the core.

For simplicity, the studied binary solid solution system was assumed to be an ideal dilute solution system, and its elastic constants and partial molar volumes are independent of the solute concentrations. Therefore, these alloy atoms can be regarded as the solute and exchanged between the core and surface shell. In this case, the chemical potentials of the solute atoms in the core and surface shell can be described by[16,17,46]

$$\mu_c^s = \mu_{c,0} + RT \ln x_c^s - \bar{V}_c^s\sigma_c \quad [7]$$

$$\mu_s^s = \mu_{s,0} + RT \ln x_s^s - 2\bar{V}_s^s\sigma_s/3 \quad [8]$$

where $\mu_{c,o}$ and $\mu_{s,o}$ are the corresponding reference chemical potentials of solute atoms in the core and surface shell, respectively; R is the gas constant; and T is the absolute temperature. Here, σ_c and $\frac{2\sigma_s}{3}$ are the hydrostatic stress in the core and surface shell, respectively, which are determined by $\sigma = \frac{1}{3}\sum_{i=1}^{3}\sigma_{ii}$. The compression is assumed to be negative, whereas tension is assumed to be positive. The compressive and tensile stresses have different effects on atom diffusion behaviors. The density functional theory (DFT) calculations[47] confirmed that the solution energy of the H atom in bcc-Fe increased with increasing 3-axis compressive strains, whereas the solution energy of the H atom decreased with increasing 3-axis tensile strains.

In the thermodynamic equilibrium, the diffusion equilibrium of solute atoms requires $\mu_c^s = \mu_s^s$. Then, the solute concentrations in the core and surface shell can be expressed as[17]

$$x_c^s = \exp\left(\frac{\Delta\mu_c^s}{RT}\right)\exp\left(\frac{\bar{V}_c^s\sigma_c}{RT}\right) = X_c^s \exp\left(\frac{\bar{V}_c^s\sigma_c}{RT}\right)$$
$$= X_c^s \exp\left(-\frac{\bar{V}_c^s\sigma_s}{RT}\frac{2\Omega_0}{R_{c,0}}\right) \quad [9]$$

$$x_s^s = x_c^s \exp\left(\frac{\Delta\mu_0^s - \bar{V}_c^s\sigma_c + 2\bar{V}_s^s\sigma_s/3}{RT}\right)$$
$$= x_c^s \exp\left(\frac{\Delta\mu_0^s + 2\sigma_s(\bar{V}_c^s\Omega_0/R_{c,0} + \bar{V}_s^s/3)}{RT}\right) \quad [10]$$

where $\Delta\mu_c^s = \mu_c^s - \mu_{c,0}$, $\Delta\mu_0^s = -(\mu_{s,0} - \mu_{c,0})$, $\sigma_c = -\frac{2\Omega_0}{R_{c,0}}\sigma_s$, and $X_c^s = \exp\left(\frac{\Delta\mu_c^s}{RT}\right)$ is the solute concentration in the core of bulk materials. For bulk materials, $\Omega_0/R_{c,0} \ll 1$, and the lattice stress in the core approaches zero. According to Eqs. 2 and 10, the surface stress and the solute concentration in the surface shell of bulk solid solution reduces to

$$\sigma_s^{bulk} = \sigma_s^0 + \frac{Y_s^s}{3}\left(\frac{\bar{V}_c^s}{\underline{V}_c}\frac{X_c^s}{1-X_c^s} - \frac{\bar{V}_s^s}{\underline{V}_s}\frac{X_s^s}{1-X_s^s}\right) \quad [11]$$

$$X_s^s = X_c^s \exp\left(\frac{\Delta\mu_0^s + 2\bar{V}_s^s\sigma_s^{bulk}/3}{RT}\right) \quad [12]$$

The apparent solute concentration of nanoparticles is usually defined as $x^s = n^s/(n^s + n)$, where $n^s = n_c^s + n_s^s$ and $n = n_c + n_s$ are the total mole numbers of solute and basis solvent atoms in the nanoparticle, respectively. Then, according to the solute conservation, the expression of $n^s = n_c^s + n_s^s$ can be written as[17]

$$\frac{x^s}{1-x^s}\left(\frac{V_{c,0}}{\underline{V}_c} + \frac{V_{s,0}}{\underline{V}_s}\right) = \frac{x_c^s}{1-x_c^s}\frac{V_{c,0}}{\underline{V}_c} + \frac{x_s^s}{1-x_s^s}\frac{V_{s,0}}{\underline{V}_s} \quad [13]$$

By solving Eqs. 2, 10 and 13 simultaneously, we can obtain the solute concentrations and stresses of nanoparticles with given apparent concentrations.

Size-dependent Electrochemical Properties of Nanoparticles

An elementary electrochemical reaction developed on the surface of the metal electrode can be written as

$$M \leftrightarrow M^{Z+} + Ze^- \quad [14]$$

where M is the reduced state of a metal, M^{Z+} is the oxidized metal state, e^- is the electron charge, and Z is the number of transferred electrons. Here, the anodic direction is considered to be forward, and the cathodic direction is reverse. In the anodic direction, the metal ions dissolved into the electrolyte from the electrode surface and a current generated from the electrode to the electrolyte.

It is well known that there is a linear relationship between the Gibbs free energy and the pressure P of solids. Because of low compressibility, the solid volume V expanded into an exponential series with respect to pressure can be mainly described by the zero-order term. According to the Gibbs-Duhem equation,[48] $\Sigma N_i d\mu_i = -SdT + Vdp$, the linear form of the chemical potential dependent on pressure follows[38]

$$\Delta\mu = \int_{P_1}^{P_2} V(P)dP = \int_{P_1}^{P_2} V_m \exp(-\chi P)dP \approx V_m \Delta P \quad [15]$$

where V_m is the partial molar volume of the corresponding component, χ is the compressibility coefficient of the solid, and ΔP is the change in the absolute value of the hydrostatic stress. In contrast to an ideal gas system, solid materials have bonding forces between their atoms. Gutman[38] systematically discussed the compression and tension effects of the initially nondeformed body (stress-free) on the corresponding mechanochemical activity. The authors concluded that hydrostatic stresses always increase the Gibbs free energy of solids with a corresponding increase in the absolute value, regardless of the direction of mechanical force (stretching or compressing the solid).

Based on the assumption of an ideal dilute solution, the chemical potential of solvent and solute atoms can be expressed by Raoult's law and Henry's law, respectively. According to Eq. 15, the electrochemical potential[34,35,38,49] of the solvent and solute atoms in the binary solid solution electrode surface, taking the surface

stress and solute concentration into account, can be expressed as

$$\bar{\mu}^B = \mu^B + RT \ln(1 - x_s^s) + 2|\sigma_s|\,\underline{V}_s^B/3 + ZF\phi \quad [16]$$

$$\bar{\mu}^A = \mu^A + RT \ln x_s^s + 2|\sigma_s|\,\underline{V}_s^A/3 + ZF\phi \quad [17]$$

where μ is the reference chemical potential of the corresponding stress-free pure metal atoms; ϕ is the inner electrical potential of the corresponding phase; F is the Faraday constant; $\underline{V}_s$ is the partial molar volume of the corresponding atoms in the surface shell, the superscript of A and B denoting the alloying solute and basis solvent atoms, respectively; and $2|\sigma_s|/3$ is the absolute value of hydrostatic stress in the surface shell. For a binary solid solution, the solute concentration is $x_s^A = x_s^s$, whereas the solvent concentration is $x_s^B = 1 - x_s^s$. Because the surface stress exists only in the surface shell of the metal electrode, the surface stress and solute concentration have no effect on the ions in the electrolyte phase.

In the equilibrium state, the total Gibbs free energy change in Eq. 14 $\Delta G = 0$.[34,35] Consequently, the corresponding equilibrium potential[34,35,38] of these electrode reactions developed on the surface of binary solid solution can be written as

$$\overrightarrow{\phi}_e^B = \phi_M - \phi_{sol} = \phi_e^B - \frac{RT \ln(1 - x_s^s) + 2|\sigma_s|\,\underline{V}_s^B/3}{ZF} \quad [18]$$

$$\overrightarrow{\phi}_e^A = \phi_M - \phi_{sol} = \phi_e^A - \frac{RT \ln x_s^s + 2|\sigma_s|\,\underline{V}_s^A/3}{ZF} \quad [19]$$

where $\phi_e = (\mu_{M^{Z+}} + Z\mu_{e^-} - \mu_M)/(ZF)$ is the equilibrium potential of the corresponding pure bulk materials neglecting their surface stress. Then, the difference in the equilibrium potential between the solvent and solute atoms in the surface shell of binary solid solution can be expressed as

$$\Delta\overrightarrow{\phi}_e^{AB} = (\phi_e^B - \phi_e^A) + \frac{1}{ZF}\left(RT \ln \frac{x_s^s}{1-x_s^s} + \frac{2|\sigma_s|(\underline{V}_s^A - \underline{V}_s^B)}{3}\right) \quad [20]$$

As all we know, if $\Delta\overrightarrow{\phi}_e^{AB} \neq 0$, anodic polarization will occur in the lower potential atom phase and cathodic polarization will occur in the higher potential atom phase. That implies that the anodic corrosion in the lower potential atom phase occurs more quickly, while the corrosion in the higher potential atom phase is inhibited, resulting in selective corrosion or galvanic corrosion. Many researchers have systematically studied selective corrosions, such as brass dezincification corrosion.[28-32] Numerous theories have been proposed that may ultimately be categorized into two groups: the selective corrosion of the less noble constituent and dissolution of both alloy constituents followed by redeposition of the more noble species. Regardless of the selective corrosion or dissolution-redeposition mechanism, the key point is that zinc preferentially leached when dezincification occurred. Therefore, we can conclude that if $\Delta\overrightarrow{\phi}_e^{AB} \geq 0$, the alloying solute atoms tend to be dissolved first, and if $\Delta\overrightarrow{\phi}_e^{AB} < 0$, the basis solvent atoms tend to be dissolved first. With increasing absolute value $|\Delta\overrightarrow{\phi}_e^{AB}|$, the selective corrosion process tends to be easier.

In the presence of mechanical deformation and alloying atoms, there would be a shift in the chemical/electrochemical potential of both components based on Eqs. 16 and 17, denoted as $(RT \ln x_s + 2|\sigma_s|\,\underline{V}_s/3)$. Moreover, the electrode polarization of $\Delta\phi$ in an electrode reaction, equal to the variation in overpotential, will lead to a change in the atomic potential in the metal by $\alpha\Delta\phi$ and the potential of the metal ions dissolved in the electrolyte by $-\beta\Delta\phi$.[34,35] In most cases, $\alpha + \beta = 1$, where α and β are the transfer coefficients of the electrochemical reaction. Correspondingly, the activation energy barriers ΔG_f^a and ΔG_r^a of the electrode reaction for the dissolved component are given as

$$\Delta \overrightarrow{G_f^a} = \Delta \overrightarrow{G_0^a} - \alpha(ZF\eta + RT \ln x_s + 2|\sigma_s| \, \underline{V}_s/3) \qquad [21]$$

$$\Delta \overleftarrow{G_r^a} = \Delta \overleftarrow{G_0^a} + (1 - \alpha)(ZF\eta + RT \ln x_s + 2|\sigma_s| \, \underline{V}_s/3) \quad [22]$$

where $\Delta \overrightarrow{G_0^a}$ and $\Delta \overleftarrow{G_0^a}$ are the activation energy barriers of the oxidation and reduction reactions of corresponding strain-free pure bulk metal ignoring the surface stress, respectively, developed on the equilibrium potential ϕ_e, and η is the overpotential. Therefore, based on the Butler-Volmer equation,[34–37]

$$\overrightarrow{j_f} = ZF\vec{k}\vec{a} \exp\left(-\frac{\Delta \overrightarrow{G_f^a}}{RT}\right)$$

$$= j_0 \exp\left(\frac{\alpha(ZF\eta + RT \ln x_s + 2|\sigma_s| \, \underline{V}_s/3)}{RT}\right) \qquad [23]$$

$$\overleftarrow{j_r} = ZF\overleftarrow{k}\overleftarrow{a} \exp\left(-\frac{\Delta \overleftarrow{G_r^a}}{RT}\right)$$

$$= j_0 \exp\left(-\frac{(1 - \alpha)(ZF\eta + RT \ln x_s + 2|\sigma_s| \, \underline{V}_s/3)}{RT}\right) \qquad [24]$$

where $j_0 = ZFKa = ZFka \exp\left(-\frac{\Delta G_0^a}{RT}\right)$ is the exchange current density of the strain-free pure bulk metal neglecting surface stress when the electrode reaction developed on the equilibrium potential ϕ_e ($\eta = 0$ and $j_f = j_r = j_0$), K is the rate constant, k is the pre-exponential factor, and ΔG_0^a is the forward or reverse activation energy barrier. Therefore, the net corrosion current density of the electrode reactions for the dissolved component of the solid solution particle can be expressed by $\overrightarrow{J} = \overrightarrow{j_f} - \overrightarrow{j_r}$. Obviously, these electrochemical properties discussed above are a function of the surface stress and component concentrations will also be size-dependent.

For bulk solid solution materials, the surface stress σ_s was reduced to σ_s^{bulk}, and the corresponding component concentration of surface shell x_s was reduced to X_s. Consequently, substituting them into Eqs. 18 and 24, we can obtain the equilibrium potential and the current density of bulk solid solution electrode reactions.

Numerical Analysis

Here, binary solid solution particles of CuZn were introduced to illustrate the size-dependent mechanical and electrochemical properties. These studies were conducted on CuZn particles, including apparent Zn concentrations of 5%, 10%, 15%, 20% and 25%. Many experimental results have confirmed that dezincification corrosion will occur in the bulk single phase α brass when the concentration of Zn is larger than 20%. Based on the binary solid solution nanoparticle model discussed above, the elastic constants and partial molar volumes are independent of the solute concentrations. For simplicity, the biaxial eigenstress $\sigma_s^0 = 1.38$ GPa and biaxial surface modulus $Y_s^s = 125.43$ GPa of pure Cu, which came from our previous work,[49] were employed to study the CuZn particles. The bulk triaxial Young's modulus was obtained similar to the bulk biaxial Young's modulus.[49] A representative domain of $8 \times 8 \times 8$ unit cells with periodic boundary conditions in all three directions was adopted to simulate the bulk material triaxial compressive and tensile tests. The bulk triaxial Young's modulus $K_c^s = 138.52$ GPa of pure Cu was calculated from the second derivatives of the bulk strain energy density with respect to the applied bulk strain. The solute atoms of Zn have an *hcp* structure with an atomic radius of 1.38 Å, lattice constants of $a = 2.66$ Å and $c = 4.95$ Å, a molar volume of $V_m^{Zn} = 9.13 \times 10^{-6}$ m^3 mol^{-1}, and the surface stress of bulk Zn is 0.8 GPa. Based on the studies of Zhang,[17] we made the following assumptions for the binary CuZn solid solution studies: $T = 300$ K, $\Omega_0 = 1$ nm, $\Delta\mu_0^s = 10$ kJ mol^{-1}, $\underline{V}_c = V_m^{Cu} = 7.14 \times 10^{-6}$ m^3 mol^{-1}, $\underline{V}_s = 1.1\underline{V}_c = 7.85 \times 10^{-6}$ m^3 mol^{-1}, $\bar{V}_c^s = V_m^{Zn} = 9.13 \times 10^{-6}$ m^3 mol^{-1}, and $\bar{V}_s^s = 0.9\bar{V}_c^s = 8.217 \times 10^{-6}$ m^3 mol^{-1}. Because theoretical calculations and experimental observations have been confirmed and widely accepted, the thickness variations in similar structure grain boundaries are within the range of 0.4 to 2.0 nm.[50–53] Hence, the surface shell thickness of particles was assumed to be 1 nm hereinafter. All these parameters and their corresponding values used in the numerical analysis were summarized in the Table I. The transfer coefficients of the electrochemical reactions were assumed to be $\alpha = \beta = 0.5$.

Size-dependent stresses and solute concentrations in the CuZn nanoparticles. — Then, substituting the CuZn binary solid solution properties listed above and solving Eqs. 2 and 13 simultaneously, the stresses and solute concentrations of the surface shell and core can be determined. The variations in the stresses in the surface and core of CuZn binary solid solution nanoparticles vs the changing radius and apparent Zn concentrations (5%, 10%, 15%, 20% and 25%) are shown in Figs. 1a and 1b, respectively. These binary solid solution particles exhibit the same trend. When the particle radius is sufficiently large, the stress in the core approaches zero independence of the apparent Zn concentrations, whereas the surface stress approaches the bulk surface stress, which is dependent on the apparent Zn concentrations of the CuZn binary solid solution. Moreover, as the nanoparticle radius decreases, the stress in the core and surface shell exhibits the opposite trend. With decreasing nanoparticle radius, the relaxation magnitude and the stress in the core increase, whereas the surface stress decreases remarkably. Obviously, these apparent Zn concentrations have almost no effect on the stress in the core, but the surface stresses of a given radius increases with increasing apparent Zn concentrations from 5% to 25%.

The solute Zn concentrations in the surface shell x_s^s and core x_c^s and their ratios (x_s^s/x_c^s) were plotted as a function of the nanoparticle radius and the apparent Zn concentrations in Figs. 2a–2c, respectively. The concentration distributions exhibit the same trend for all CuZn particles. The Zn concentrations in the surface shell x_s^s and core x_c^s both decreased with decreasing nanoparticle radius and increased with increasing apparent Zn concentration. The ratios x_s^s/x_c^s increased with decreasing nanoparticle radius and increased with decreasing apparent Zn concentration. Thus, the difference in the solute Zn concentrations between the surface shell and core increased with decreasing CuZn nanoparticle radius, and their magnitude increased with decreasing apparent Zn concentration. This phenomenon occurs because the stresses in the surface shell and core exhibit a different trend with decreasing nanoparticle radius.

Table I. The parameters and values used in the numerical analysis.

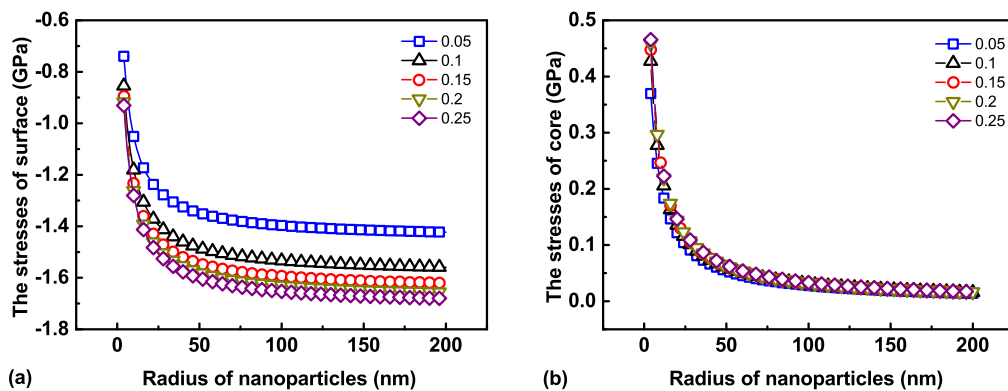| Parameters	Values	References	Parameters	Values	References
σ_s^0/GPa	1.38	49	K_c^s/GPa	138.52	
Y_s^s/GPa	125.43	49	$\Delta\mu_0^s$/kJ/mol	10	17
$\underline{V}_c$/m^3/mol	7.14×10^{-6}		$\bar{V}_c^s$/m^3/mol	9.13×10^{-6}	
$\underline{V}_s$/m^3/mol	7.85×10^{-6}		$\bar{V}_s^s$/m^3/mol	8.217×10^{-6}	
V_m^{Zn}/m^3/mol	9.13×10^{-6}		Ω_0/nm	1	17, 50–53
σ_{bulk}^{Zn}/GPa	0.8		T/K	300	

Figure 1. Variations in the stresses in the surface shell (a) and the stresses in the core (b) as a function of the CuZn binary solid solution nanoparticle radius and the apparent Zn concentration.
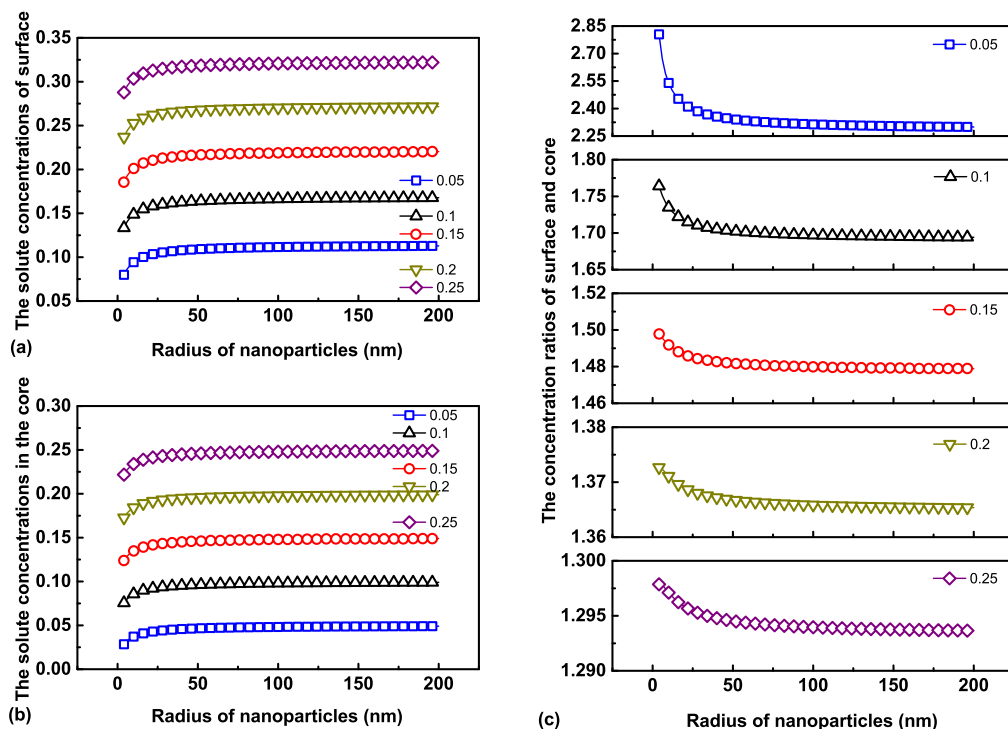

Figure 2. Variations in the Zn concentrations in the surface shell $x_s{}^s$ (a), the Zn concentrations in the core $x_c{}^s$ (b) and the Zn concentration ratios between surface shell and core (x_s^s/x_c^s) (c) as a function of the CuZn binary solid solution nanoparticle radius and the apparent Zn concentration.

The larger the magnitude of the solute segregation in nanoparticles is, the smaller the stress difference between the surface shell and core.

Size-dependent electrochemical properties of CuZn nanoparticles.—Here, the electrode reactions developed on the CuZn solid solution particle surface were assumed to be $Zn \leftrightarrow Zn^{2+} + 2e^-$ and $Cu \leftrightarrow Cu^{2+} + 2e^-$ for each component, and their standard electrode potentials were assumed to be the equilibrium potential of the corresponding bulk $\phi_e^{Zn} = -0.762$ V and $\phi_e^{Cu} = 0.345$ V (referenced to the standard hydrogen electrode), respectively. Then, according to Eq. 20, the difference in the equilibrium potential between the Cu and Zn atoms in the surface shell of CuZn nanoparticles, taking into account the surface stress and solute Zn segregation effects, are shown in Fig. 3 as a function of the nanoparticle radius and the apparent Zn concentration. The values of the equilibrium potential difference decreased with decreasing nanoparticle radius but increased with increasing apparent Zn concentration. The variation range of the equilibrium potential difference decreased with increasing apparent Zn concentration. When the particle radius was

less than 25 nm, the equilibrium potential difference between the Cu and Zn atoms in the surface shell decreased sharply with decreasing radius. When the particle radius was larger than 100 nm, the equilibrium potential difference gradually tended to a constant value depending on the apparent Zn concentration. In general, the equilibrium potential difference between the solvent and solute atoms in the surface shell can be regarded as the driving force of selective corrosion on binary solid solutions.

According to Eqs. 18 and 19, the expression of the equilibrium potential difference between the dissolved component of binary solid solution particles and the pure bulk material of the corresponding component, taking into account the surface stress and solute segregation effects, can be given as

$$\Delta \overleftrightarrow{\phi_e} = \overleftrightarrow{\phi_e}^{particle} - \overleftrightarrow{\phi_e}^{bulk} = -\frac{RT \ln x_s + 2(|\sigma_s| - |\sigma_s^{bulk}|)\underline{V}_s/3}{ZF}$$

[25]

The variations in the equilibrium potential difference denoted by Eq. 25 are shown in Fig. 4 as a function of the nanoparticle radius
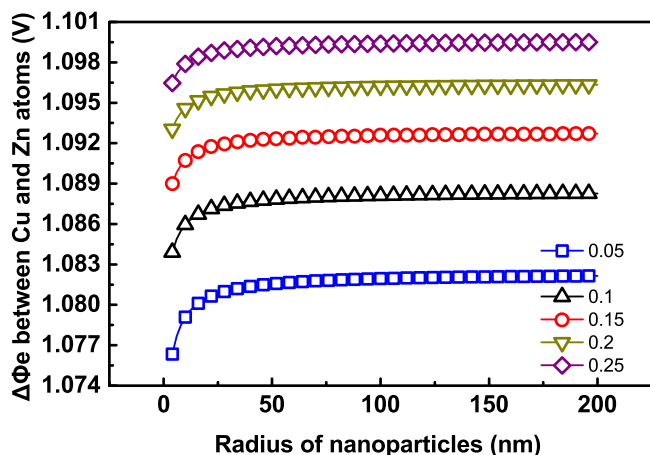
Figure 3. Variations in the equilibrium potential difference between the Cu and Zn atoms in the surface shell of CuZn binary solid solution nanoparticle as a function of the nanoparticle radius and the apparent Zn concentration.
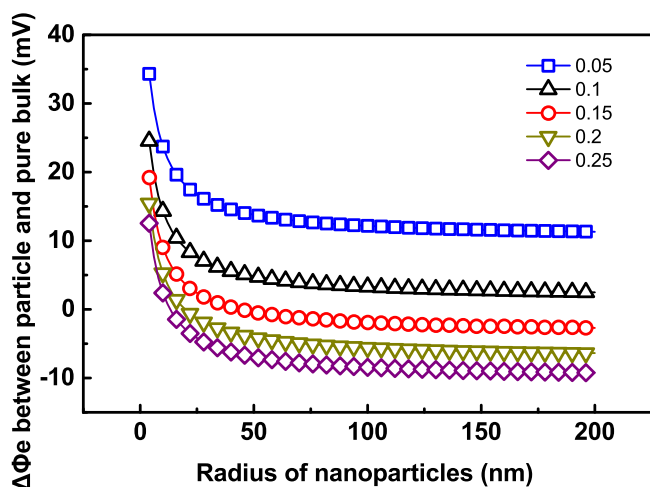

Figure 4. Variations in the equilibrium potential difference between the dissolved Zn atoms in the CuZn nanoparticles and the pure bulk Zn as a function of the nanoparticle radius and the apparent Zn concentration.

and the apparent Zn concentration. Obviously, these CuZn binary solid solution particles exhibit the same trend, and the values of the equilibrium potential difference increased with decreasing nanoparticle radius but decreased with increasing apparent Zn concentration.
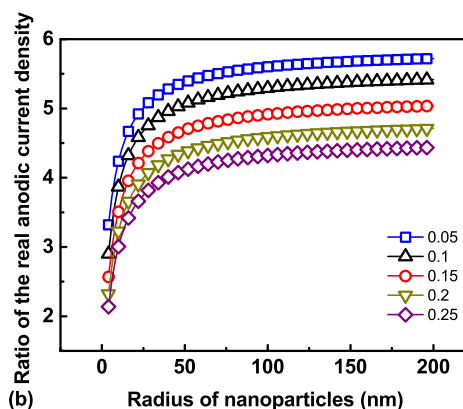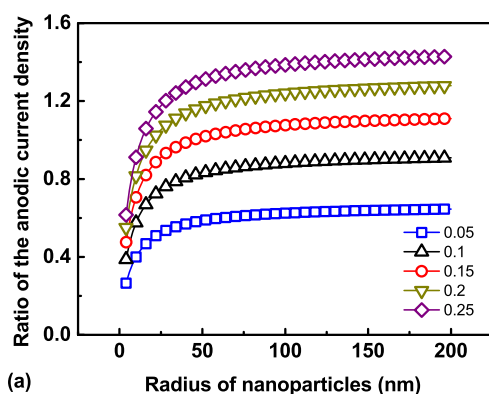
With decreasing equilibrium potential difference, the electrochemical activity of the corresponding component increased. Therefore, with increasing apparent Zn concentration, the selective corrosion of Zn in the nanoparticles tended to be enhanced. However, for a given apparent Zn concentration, the selective corrosion of Zn decreased with decreasing nanoparticle radius.

These electrochemical reactions developed on CuZn nanoparticles were assumed with high anodic polarizations and the same overpotential of η, in which the cathodic reaction rate were small enough to be ignored and the corrosion current density approximate to the anodic current density. Then, according to Eq. 23, the accurate expression of the anodic current density ratio between the dissolved component of the binary solid solution particles and the pure bulk material of the corresponding component, taking into account the surface stress and solute segregation effects, can be given as

$$\frac{\overleftrightarrow{j}_f^{particle}}{\overleftrightarrow{j}_f^{bulk}} = \exp\left(\frac{\alpha\{RT \ln x_s + 2(|\sigma_s| - |\sigma_s^{bulk}|)\underline{V}_s/3\}}{RT}\right) \quad [26]$$

Because these solute atoms are uniformly distributed in the surface shell of binary solid solutions, the surface occupancies of solute atoms should approximate the corresponding surface concentration of nanoparticles. Then, based on Eq. 26 and the surface occupancies of the dissolved component in the nanoparticles x_s, we can obtain the ratio of the real anodic current density between the dissolved component of the binary solid solution particles and the pure bulk material of the corresponding component.

$$Ratio_{real} = \frac{\overleftrightarrow{j}_f^{particle} \Big/ x_s}{\overleftrightarrow{j}_f^{bulk}} \quad [27]$$

The variations in the ratio of the anodic current density and the ratio of the real anodic current density given by Eqs. 26 and 27 are shown in Figs. 5a and 5b as a function of the nanoparticle radius and the apparent Zn concentration, respectively. Obviously, in these CuZn particles, the values of the ratio of the anodic current density and the ratio of the real anodic current density both decreased with decreasing nanoparticle radius. Therefore, for a given apparent Zn concentration, the selective corrosion of Zn decreased with decreasing nanoparticle radius, meaning that the stability was enhanced in their thermodynamic equilibrium state which qualitatively consistent with the Cu[42] and Ag[43] nanoparticles. The tip-induced Cu clusters on Au(111) surface with an average height of 0.6 nm and a width of 3.2 nm were observed that the dissolution starts at about +40 mV vs Cu/Cu^{2+}.[42] However, the electrochemically grown large copper clusters readily dissolved at +10 mV vs Cu/Cu^{2+}. The dissolution potential of nanoscale tip-induced Cu cluster increased

(a)

(b)

Figure 5. Variations in the ratio of the anodic current density (a) and the ratio of the real anodic current density (b) between the dissolved Zn atoms in the CuZn nanoparticles and the pure bulk Zn as a function of the nanoparticle radius and the apparent Zn concentration.

30 mV compared to that of large copper clusters, which consistent well with our calculations that the equilibrium potential of CuZn nanoparticles increased almost 25 mV compared to that of pure bulk Zn. The anodic dissolution of silver particles on highly oriented pyrolytic graphite (HOPG) electrode surfaces was investigated.[43] The silver particles larger than 20 nm in diameter were dissolved from a high cluster density of $\sim 10^9$ cm^{-2} to zero in 10 min, however, these silver clusters with subnanometer of 0.3–0.6 nm were dissolved in an hour. Compared with these silver particles larger than 20 nm in diameter, the dissolution rate of subnanometer particles reduced to 1/6. Which is qualitatively consistent with our calculations that the anodic current density of CuZn particles reduced to $1/3 \sim 1/2$ with the radius decreased from 200 nm to 2 nm. Moreover, the small clusters of copper can be arranged on gold surfaces by the tip of a scanning tunneling microscope (STM) and revealed a surprisingly high stability against anodic dissolution.[54–56]

The anodic current density ratio increased with increasing apparent Zn concentration, implying that with increasing apparent Zn concentration, the selective corrosion of Zn in the nanoparticles tended to be enhanced. However, the ratio of the real anodic current density increased with decreasing apparent Zn concentration, indicating that with decreasing surface occupancies of the anodic phase, the magnitude of selective corrosion damage will be enhanced. These results were qualitatively consistent with brass dezincification corrosions.[28–32] When the particle radius was less than 25 nm, the electrochemical properties of the CuZn binary solid solution nanoparticles varied sharply with increasing radius. Then, these values of nanoparticles gradually approached a constant that depended on the apparent Zn concentration when the particle radius was larger than 100 nm.

Conclusions

In the present work, the size-dependent electrochemical properties of nanoparticles and the effects of size-dependent stresses and solute concentration distributions were discussed based on the thermodynamic equilibrium theory. The spherical nanoparticles of binary solid solution were modeled as a core–shell structure. Finally, by combining the generalized capillary equation with the Gibbs-Duhem equation and the Butler-Volmer equation, a size-dependent model was obtained and can be used to simultaneously analyze nanoparticle size, stresses, solute segregation and electrochemical properties in solid solution nanoparticles.

Our numerical analysis showed that the CuZn binary solid solution particles exhibit the same trend: as the nanoparticle radius decreased, the surface stress decreased, whereas the stress in the core and the solute segregation of Zn increased. The smaller the apparent Zn concentration of nanoparticles was, the higher the magnitude of Zn segregation. The larger the magnitude of the Zn segregation in the nanoparticles was, the smaller the stress difference between the surface shell and core. With decreasing CuZn nanoparticle radius, the anodic current density decreased, whereas the equilibrium potential increased, meaning that the stability was enhanced in their thermodynamic equilibrium state. As the apparent Zn concentration increased, the equilibrium potential decreased, but the anodic current density and the equilibrium potential difference between the CuZn nanoparticles' components increased, implying that the nanoparticle selective corrosion of Zn atoms tended to be enhanced. These results were qualitatively consistent with some experimental observations.

Acknowledgments

References

1. R. Shuttleworth, *Proc. Phys. Soc. A*, **63**, 444 (1950).
2. E. Orowan, *Proc. R. Soc. London, Ser. A*, **316**, 473 (1970).
3. J. Diao, K. Gall, M. L. Dunn, and J. A. Zimmerman, *Acta Mater.*, **54**, 643 (2006).
4. H. Liang, M. Upmanyu, and H. Huang, *Phys. Rev. B*, **71**, 241403 (2005).
5. T. Y. Zhang, M. Luo, and W. K. Chan, *J. Appl. Phys.*, **103**, 104308 (2008).
6. R. Dingreville, J. Qu, and C. Mohammed, *J. Mech. Phys. Solids*, **53**, 1827 (2005).
7. R. Dingreville and J. Qu, *Acta Mater.*, **55**, 141 (2007).
8. T.-Y. Zhang, Z.-J. Wang, and W.-K. Chan, *Phys. Rev. B*, **81**, 195427 (2010).
9. M. Yamauchi, R. Ikeda, H. Kitagawa, and M. Takata, *J. Phys. Chem. C*, **112**, 3294 (2008).
10. C. Sachs, A. Pundt, R. Kirchheim, M. Winter, M. T. Reetz, and D. Fritsch, *Phys. Rev. B*, **64**, 075408 (2001).
11. C. Langhammer, V. P. Zhdanov, I. Zorić, and B. Kasemo, *Chem. Phys. Lett.*, **488**, 62 (2010).
12. E. A. Sutter and P. W. Sutter, *J. Mater. Sci.*, **46**, 7090 (2011).
13. H. Mori and H. Yasuda, *Bull. Mater. Sci.*, **22**, 181 (1999).
14. C. Srivastava, S. Chithra, K. D. Malviya, S. K. Sinha, and K. Chattopadhyay, *Acta Mater.*, **59**, 6501 (2011).
15. N. Meethong, H.-Y. S. Huang, W. C. Carter, and Y.-M. Chiang, *Electrochem. Solid-State Lett.*, **10**, A134 (2007).
16. T.-Y. Zhang and H. Ren, *Acta Mater.*, **61**, 477 (2013).
17. T. Y. Zhang and H. Ren, *J. Therm. Stresses*, **36**, 626 (2013).
18. P. H. Robbs and N. V. Rees, *PCCP*, **18**, 24812 (2016).
19. K. Z. Brainina, L. G. Galperin, V. Vikulova, and A. L. Galperin, *J. Solid State Electrochem.*, **17**, 43 (2013).
20. X. Y. Wang and D. Y. Li, *Electrochim. Acta*, **47**, 3939 (2002).
21. X. Y. Wang and D. Y. Li, *Wear*, **255**, 836 (2003).
22. V. Afshari and C. Dehghanian, *Corros. Sci.*, **51**, 1844 (2009).
23. V. Afshari and C. Dehghanian, *Mater. Chem. Phys.*, **124**, 466 (2010).
24. R. Mishra and R. Balasubramaniam, *Corros. Sci.*, **46**, 3019 (2004).
25. R. A. Masitas and F. P. Zamborini, *J. Am. Chem. Soc.*, **134**, 5014 (2012).
26. M. D. Popolo, E. Leiva, H. Kleine, J. Meier, U. Stimming, M. Mariscal, and W. Schmickler, *Appl. Phys. Lett.*, **81**, 2635 (2002).
27. R. Inturi and Z. Szklarska-Smialowska, *Corrosion*, **48**, 398 (1992).
28. P. Zhou, M. J. Hutchison, J. W. Erning, J. R. Scully, and K. Ogle, *Electrochim. Acta*, **229**, 141 (2017).
29. E. Sarver, Y. Zhang, and M. Edwards, "Review of brass dezincification corrosion in potable water systems." *Corros. Rev.*, **28**, 155 (2010).
30. S. Selvaraj, S. Ponmariappan, M. Natesan, and N. Palaniswamy, "Dezincification of Brass and its Control—An Overview." *Corros. Rev.*, **21**, 41 (2003).
31. R. H. Heidersbach and E. D. Verink, *Corrosion*, **28**, 397 (1972).
32. H. Sugawara and H. Ebiko, *Corros. Sci.*, **7**, 513 (1967).
33. J. A. V. Butler, *Trans. Faraday Society*, **19**, 734 (1924).
34. J. M. Bockris and A. K. Reddy, in *Modern Electrochemistry: an Introduction to an Interdisciplinary Area.* (Plenum Publishing Corportation, New York) (1970).
35. J. Koryta, J. Dvorak, and A. M. Bond, in *Principles of Electrochemistry* (Wiley, New York) (1987).
36. A. J. Bard and L. R. Faulkner, in *Electrochemical Methods: Fundamentals and Applications* (Wiley, New York) 2nd ed. (2000).
37. D. Ken A and S. Bromberg, in *Molecular Driving Forces: Statistical Thermodynamics in Chemistry and Biology* (Garland Science, New York) (2003).
38. E. M. Gutman, in *Mechanochemistry of Materials* (Cambridge Int. Science Publishing, Cambridge) (1998).
39. M. Ganser, F. E. Hildebrand, M. Klinsmann, M. Hanauer, M. Kamlah, and R. M. McMeeking, *J. Electrochem. Soc.*, **166**, H167 (2019).
40. F. Yang, *Sci. Chin. Phys. Mech. Astron.*, **59**, 114611 (2016).
41. A. Barbucci, G. Farne, P. Matteazzi, R. Riccieri, and G. Cerisola, *Corros. Sci.*, **41**, 463 (1998).
42. D. M. Kolb, G. E. Engelmann, and J. C. Ziegler, *Angew. Chem. Int. Ed.*, **39**, 1123 (2000).
43. K. H. Ng, H. Liu, and R. M. Penner, *Langmuir*, **16**, 4016 (2000).
44. J. Weissmüller and J. W. Cahn, *Acta Mater.*, **45**, 1899 (1997).
45. J. Weissmüller, H. L. Duan, and D. Farkas, *Acta Mater.*, **58**, 1 (2009).
46. P. Gao, H. Ma, Q. Wu, L. Qiao, A. A. Volinsky, and Y. Su, *J. Phys. Chem. C*, **120**, 17613 (2016).
47. X. Li, C. Gao, X. L. Xiong, Y. Bai, and Y. J. Su, *Int. J. Hydrogen Energy*, **40**, 10340 (2015).
48. G. B. McFadden and A. Wheeler, *Proc. R. Soc. London, Ser. A*, **458**, 1129 (2002).
49. H. Ma, X. Xiong, P. Gao, X. Li, Y. Yan, A. A. Volinsky, and Y. Su, *Sci. Rep.*, **6**, 26897 (2016).
50. O. Yeheskel, R. Chaim, Z. Shen, and M. Nygren, *J. Mater. Res.*, **20**, 719 (2005).
51. H. Marquardt, A. Gleason, K. Marquardt, S. Speziale, L. Miyagi, G. Neusser, H.-R. Wenk, and R. Jeanloz, *Phys. Rev. B*, **84**, 064131 (2011).
52. L. Zhu and X. Zheng, *Acta Mech.*, **213**, 223 (2010).
53. R. Chaim, *J. Mater. Res.*, **12**, 1828 (1997).
54. D. M. Kolb, R. Ullmann, and J. C. Ziegler, *Electrochim. Acta*, **43**, 2751 (1998).
55. D. M. Kolb, G. E. Engelmann, and J. C. Ziegler, *Solid State Ionics*, **131**, 69 (2000).
56. R. Ullmann, T. Will, and D. M. Kolb, *Ber. Bunsenges. Phys. Chem.*, **99**, 1414 (1995).